An optical platform for the production, trapping, manipulation and visualization of ultra-low interfacial tension emulsion droplets

Hargreaves, Alexander, Kirby, Andrew, Bain, Colin, Love, Gordon, Bolognesi, Guido, et al.

Alexander L. Hargreaves, Andrew K. Kirby, Colin D. Bain, Gordon D. Love, Guido Bolognesi, Oscar Ces, Mark Neil, Andrew D. Ward, "An optical platform for the production, trapping, manipulation and visualization of ultra-low interfacial tension emulsion droplets," Proc. SPIE 8810, Optical Trapping and Optical Micromanipulation X, 88101W (12 September 2013); doi: 10.1117/12.2027105

SPIE.

Event: SPIE NanoScience + Engineering, 2013, San Diego, California, United States

An optical platform for the production, trapping, manipulation and visualization of ultra-low interfacial tension emulsion droplets

Alexander L. Hargreaves[a], Andrew K. Kirby[a], Colin D. Bain*[a], Gordon D. Love[a], Guido Bolognesi[b], Oscar Ces[b], Mark Neil[b] and Andrew. D. Ward[c].
[a]Department of Chemistry, University of Durham, South Road, Durham, UK, DH1 3LE;
[b]Department of Chemistry, Imperial College London, Exhibition Road, London, UK, SW7 2AZ;
[c]Rutherford Appleton Laboratory, Chilton, Oxon, UK, OX11 0QX.

ABSTRACT

We discuss the design, implementation and performance of a novel platform for the production and optical control of ultra-low interfacial tension droplets in the 1-10 micron regime. A custom-designed, integrated microfluidic system allows the production of oil-in-water emulsion droplets of controllable size. This provides an optimised physical platform in which individual droplets are selected, trapped and shaped by holographic optical tweezers (HOTs) via extended optical landscaping. The 3D structure of the shaped droplet is interrogated by a combination of conventional brightfield imaging and fluorescent structured-illumination sectioning. We detail the problems and limitations of closed-loop holographic control of droplet shape.

Keywords: Emulsion, holographic optical tweezers, ultralow interfacial tension, microfluidic, flow focusing, optical landscaping, Raman tweezers, structured illumination

1. INTRODUCTION

Consider the following techniques as employed at the micron scale: holographic optical tweezers (HOTs), fluorescence microscopy, Raman microscopy, and photopolymerisation. Taken alone, these are all proven concepts for the capture, manipulation, chemical assessment and fixation of microparticles. Microfluidic devices can produce such particles with bespoke size and chemical properties quickly, reproducibly and from a wide range of materials. Not only do we combine all of the above into a single instrument in this work, but add capacity also for the 3D shape reconstruction of *optically deformed* microparticles, specifically oil emulsion droplets in water.

Area-minimising surface tension always imposes a spherical free liquid interface where the effect of gravity is negligible. However, when the surface tension forces are reduced by surfactants to levels comparable with optical forces, tweezers (from points to HOT landscapes) become ideal tools for controlled deformation. Polymerisation of these shaped oil droplets will allow the user-defined morphology to be retained. Furthermore, optically generated nanothreads between microdroplets constitute a novel and highly versatile basis for the construction of 3D active nanofluidic networks, treating volumes as small as attolitres.

We discuss the microfluidic framework for production and delivery of droplets tailored to the optimal size and composition for these purposes. The required methods and experimental performance of this part of the system are detailed. Each optical technique is briefly discussed in context of recent literature, an overview of the integrated design is presented, and the problems and limitations of integration are tackled.

*c.d.bain@dur.ac.uk

Optical Trapping and Optical Micromanipulation X, edited by Kishan Dholakia, Gabriel C. Spalding,
Proc. of SPIE Vol. 8810, 88101W · © 2013 SPIE · CCC code: 0277-786X/13/$18 · doi: 10.1117/12.2027105

2. CONCEPTS AND DESIGN

2.1 Microfluidics

Droplet-based microfluidics deals with the generation, transport and manipulation of femto- to picolitre sized droplets dispersed in a continuous phase inside microfluidic devices.[1] This method, which allows the production of highly monodisperse droplet at rates up to few tens of kHz, has several advantages with respect to macroscopic emulsification approaches. Precise generation and repeatability, dimensional scaling benefits, ultra-high throughput, and a capability to compartmentalize and mimic biological and chemical reactions within individual droplets are some of the numerous advantages of droplet-based microfluidics. As a consequence, there are numerous applications[2] based on droplet microfluidics, within the chemical, physical, biological and biomedical sciences. Moreover, such microfluidic platforms are not just limited to the generation of liquid or gaseous particles, but they are also being applied for manufacturing either spherical or asymmetric solid or gel objects[3] through different means (e.g. U.V.-initiated or catalyst-initiated polymerization of liquid droplets), making this technology even more interesting in fields like drug discovery, biomedical imaging, therapeutic delivery and diagnostics.

The formation of droplets within microfluidic devices is typically based on spontaneous processes and it is generally the result of a force balance between the flow shear stresses and the interfacial tension at the liquid-liquid interface. Different channel geometries have been extensively studied for promoting droplet break-up down to moderately low surface tensions and the most popular among them are the co-flowing streams, T-junction and planar or three-dimensional flow focusing junctions.[4]

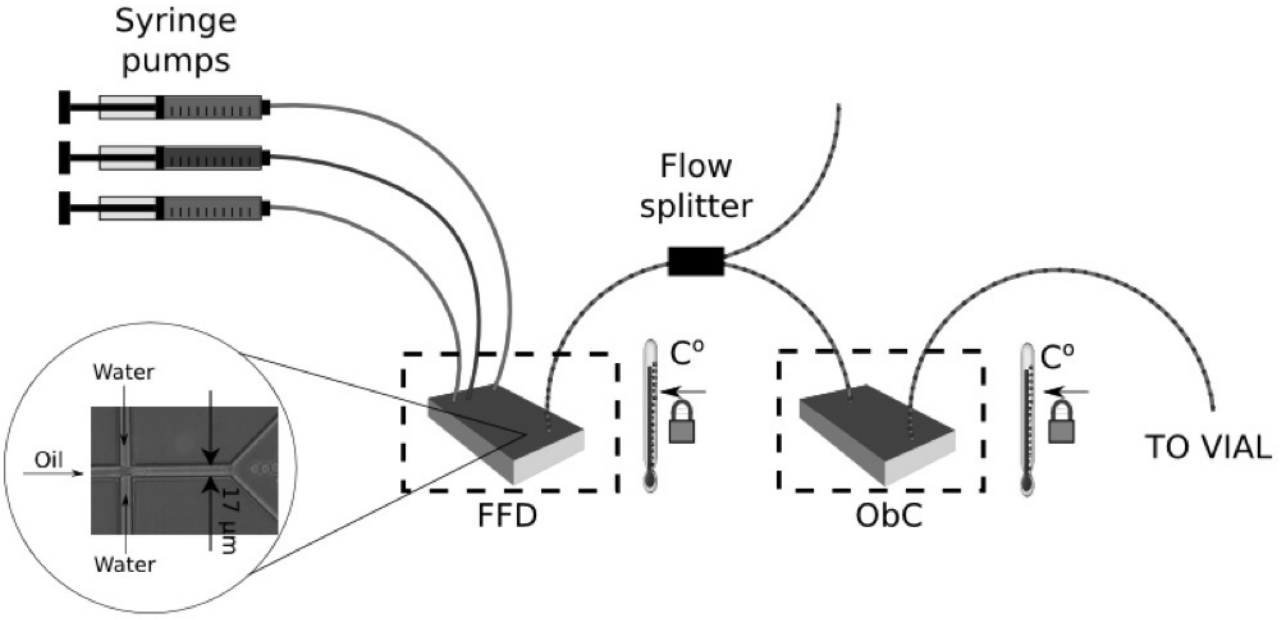

Figure 1. Scheme of the microfluidic platform for ultra-low interfacial tension droplet generation, comprising the flow focusing device (FFD) and observation chamber (ObC) for subsequent storage and manipulation. Left inset: flow focusing junction within the FFD. Outflow products are collected in a non-airtight vial.

In this research we adopt the planar flow-focusing junction for generating highly monodisperse ultra-low interfacial tension droplet (c.v. < 5%) whose diameter varies in the range of few micrometers to few tens of micrometers. On reducing the surface tension we also reduce surface effects such as Marangoni flows, which can both contribute to and detract from the stability of droplet generation. Little is known about the scope and underlying mechanics of fluid

phenomena occurring at ultra-low interfacial tension (i.e. exceptionally high capillary number). Though our strategy is to optimise selectively, rather than explore such a vast parameter space, this work may provide insight to a relatively untouched subject in microfluidics.

2.2 Optical manipulation

Ward *et al.*[8] provided a proof of concept that optical gradient forces can compete with capillary forces between immiscible fluids at ultralow surface tension. Arranging optical traps such that they provide a force differential across a droplet encourages it to deform from a sphere. Indeed even a single beam trap provides this differential along the optical axis, as proven by the reduction in apparent radius of a droplet at very high optical powers. The exact 3D structure is more difficult to decipher (§2.3). The variety in the number, separation and even optical shape of traps suggests that wide ranges of shapes are possible.

When the lowest surface tension droplets are optically pulled apart, they do not break. Instead, they remain connected by 'nanothreads' of oil with diameters <300 nm. Their aspect ratio vastly exceeds that of any previously known free liquid phenomenon; they are thought to be stabilised by the bending modulus of the molecular interface itself. The ligaments support flow from one drop to another, pumped by adjusting trap strengths. Networks of up to five drops have been realised previously.[5]

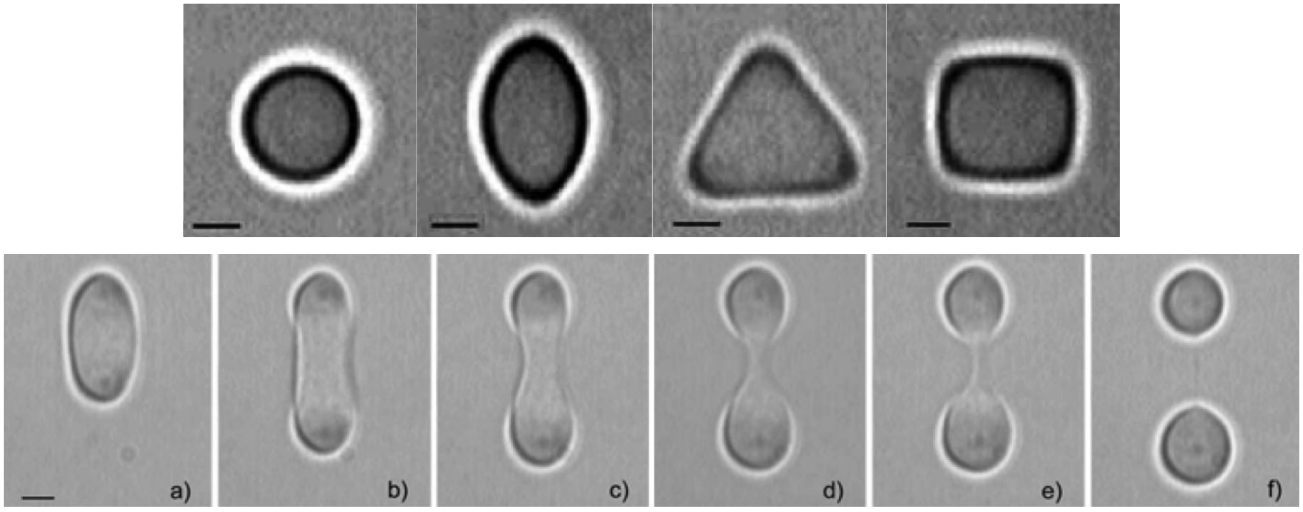

Figure 2. Previous brightfield results from a similar experimental apparatus showing optical trapping of (top, left to right) a single alkane droplet in one, two three and four coplanar traps at the droplet 'vertices'; (below, a-f) a similar droplet bifurcating across two trap positions of increasing separation until a nanothread is formed. Scale bars = 2 μm. Adapted[6] by permission of The Royal Society of Chemistry.

Custom optical tweezing is achieved in this scheme using a continuous wave Gaussian beam at 532 nm (or 1070 nm) combined with a holographic diffractive optic element and inverted microscope. The shorter wavelength is preferred as it offers higher intensity gradients and feature resolution for trapping, whilst avoiding excessive heating or photodegradation in aqueous and organic sample components respectively. We employ the phase-modulating configuration of a reflective spatial light modulator, or SLM, conjugate to the objective aperture through a lens relay as well established in optical tweezing literature.[7] Loosely, these SLMs can be thought of as miniature LCD monitors, communicating with a computer in a similar manner. Each pixel acts independently as a variable waveplate, allowing holograms to sculpt light propagating through to the object plane.

The models of SLM used herein owe their function to a layer of either ferroelectric or nematic liquid crystal. The binary ferroelectric is preferred for time-shared 'Zernike lens and prism' Gaussian traps due to its high frame rate of 2 kHz/number of trapping sites. Beamsplitters and waveplates are necessary to remove the unmodulated '0th order' beam into which most of the input light is wasted. However, the nematic model supports 8-bit blazed holograms for much higher diffractive power efficiency and holographic complexity. The typical frame rates are currently limited to video, ~40 Hz, but continue to improve.[8]

The frequency of timesharing with a conventional spherical bead is constrained weakly by the bead's simple diffusive motion. Trapping a deformable, nonspherical droplet is largely equivalent, with one exception. Even at ultralow surface tension, γ, the timescale on which an untrapped droplet regains a spherical shape is very fast: $\tau \approx \beta / \gamma \sim 10^{-3}$ s, where β is the object's drag coefficient. Thus for a given equilibrium shape, there is a minimum frequency, ~1 kHz, for timesharing traps, below which oscillations in shape are likely to occur even if the object does not diffuse away. Shaping a droplet in 3D is a thus a demanding task for timesharing multiple traps at sub-kilohertz rates. Alternatively, real-time manipulation is still achievable with algorithms such as random mask encoding[9] when only a handful of independent Gaussian traps are required. For arbitrary optical landscapes, a weighted Gerchberg-Saxton algorithm[9] can also be calculated on a high-end graphics-processing unit. Hologram-generating code also typically incorporates a user interface, which displays video superposed with interactive control of 3D trapping positions in real-time, using each of these calculation techniques as required.

2.3 Structured illumination 3D imaging

The focal planes of trapping and imaging must coincide to observe any trapped objects in detail. Even with visible achromatic objectives, these planes can be separated significantly when trapping in the infrared due to chromatic aberration. By translating relay lenses slightly along the optic axis, this condition is fulfilled. Moreover, we can use this translation effect to tune the relative location of the imaging plane *within* the trapped objects. A true representation of the 3D local structure can be obtained only if the imaging technique is spatially selective in the axial direction. From conventional images we can only constrain the 3D shape by its approximate 2D projection.

A structured illumination is used, whereby the intensity of excitation light is spatially modulated across the field of view[10]. In the returned emission, this known pattern becomes blurred under the effect of defocus (*Fig. 3*), allowing the rejection by variance threshold of only those image elements that do not correspond closely to the focal plane. Between N incremental phase-shifts of the transverse pattern, further images are taken, whose least-square deviations contribute to a complete, local z-section. If for a given pixel the intensity in each frame is represented by I_n, such that $n \le N$, this local z-section I_{XS}, is as follows[11]:

$$I_{XS} = \sqrt{\frac{\sum_{m,n \le N} \left(I_n - I_m\right)^2}{2N \sum_{n \le N} \left(\frac{I_n}{I_{WF}} - \frac{1}{2}\right)^2}} \qquad (1)$$

A set of images at many different z-sections enables viewed objects to be reconstructed in 3D. The image can be compared to the widefield image, I_{WF}, recovered by:

$$I_{WF} = \frac{1}{N} \sum_{n \le N} I_n \qquad (2)$$

The resulting focal depth resolution and image contrast depend strongly on the chosen grating period and sectioning interval.[12] Fluorescent return is preferred over brightfield output, as the possibility of self-refraction through objects of

higher refractive index is avoided. By constructing a structured epi-illumination through the objective, we retain a conventional brightfield-imaging mode for comparison.

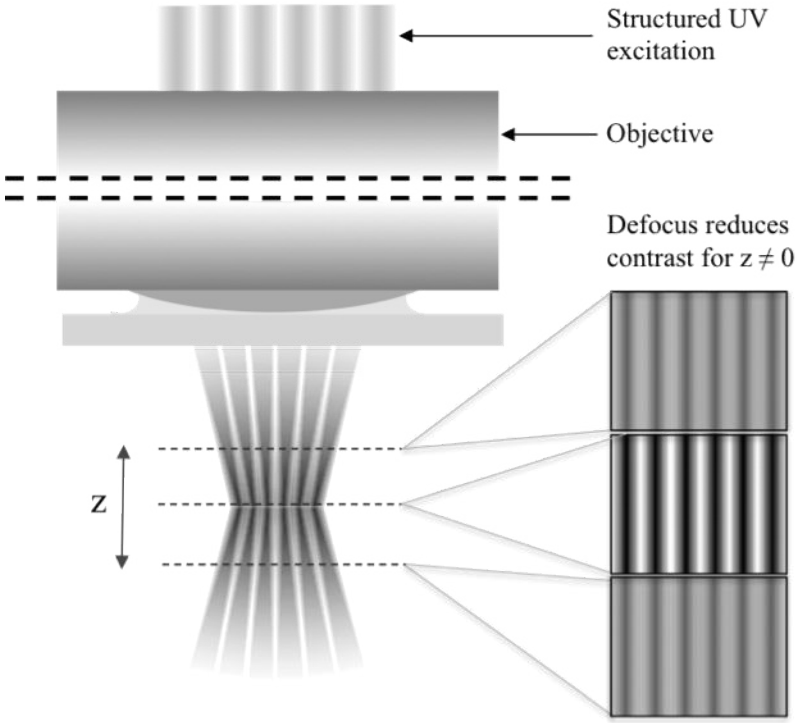

Figure 3. Principle of defocus-dependent image variance for structured illumination of a fluorescent sample, allowing discrimination of the z-section near the focus.

In this particular application to microdroplets, we might sensibly assume that there is a single extended object of constant, known volume rather than a sparse field; also this object is optically homogeneous, so we only need to identify the boundary location. Many 3D imaging techniques are capable of reconstructing such a system satisfactorily. However, fluorescent SIM does not require these assumptions. SIM is expected to yield better signal-to-noise performance[13] and sharper sectioning response than even confocal scanning microscopy. Its 3D reconstruction is superior to stereoscopic or polychromatic imaging, particularly with feature-poor or hollow shapes. The great strength of SIM is that it can resolve arbitrary volumetric distributions, as each z-section is independent. Though intended for the assessment of the microparticles discussed here, the imaging arm of our instrument can be applied to widely different target systems.

2.4 Photopolymerisation and Raman spectroscopy

Liquid droplets return to a spherical shape in the absence of optical pressure, regardless of their morphological history. For any shape memory to persist, they must be made viscoelastic or even solidified. If the droplets consist of monomer oil doped with a suitable free radical initiator, a photopolymerisation reaction can be induced *in situ* by exposure to UV light (*Fig. 4*). In order to fix a nonspherical shape of a microdroplet, the irradiation must be approximately uniform over the droplet volume, wherever it occurs in the field of view. Depending on the polymerisation rates and initiator absorbance, intensities of ~10 W cm^{-2} are required, which is difficult to achieve with a conventional UV LED. Though more expensive, a low-power laser offers more control over alignment and uniformity.

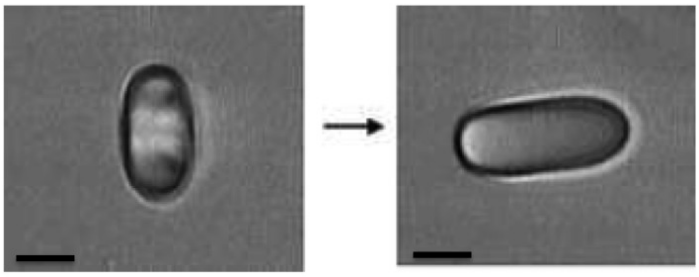

Figure 4. Previous results from a similar experimental apparatus[14] showing an optically trapped acrylate monomer microdroplet at ultralow surface tension before and after photopolymerisation (scale bars = 2 μm). Deformation is retained indefinitely after polymerisation, albeit imperfectly due to shrinkage and surface tension stresses.

We propose to follow the rate of polymerisation over the reaction *via* Raman spectroscopy with backscattered trapping laser light. For monomers with the highest propagation rates, free radical polymerisation spans only ~100 ms. Thus, spectra must be resolved quickly, on the order of 10 ms, and refined by a statistical treatment such as principal component analysis.[15] For our purposes, spatial information on droplet composition is less critical than temporal resolution. Were the acquisition timescale not a limiting factor, the composition could be mapped in strongly illuminated areas by imaging the Raman signal directly (e.g. through an étalon). However, to reduce exposure times at an acceptable level of noise, it is necessary instead to use a slit and blazed diffraction grating spectrograph, and to integrate the signal by binning pixels in the spatial dimension.

Our approach also offers spatial selectivity to the trapped object of interest. The linear intensity scaling of the Raman effect does not constrain it axially to the trapping region, since roughly the same input power is contained in each transverse beam section. Thus, scattering from a significant volume above and below the object will contribute significantly to the signal, even in aqueous media. Instead of a slit, a spectroscopic pinhole of diameter D provides the necessary confocality to exclude light originating more than a distance of order $D / 2M$ from the focus, where M is the magnification between the sample and pinhole. With an EMCCD detector, noise is usually shot-limited, so this procedure improves effective signal-to-noise.[16]

3. EXPERIMENTAL

3.1 Microfluidics

The microfluidic platform consists of two main sections: a glass flow focusing device (FFD) for droplet generation and a hybrid glass/polydymethilsiloxane (PDMS) observation chip (ObC) for droplet storage and manipulation. The oil (dispersed) and the water (continuous) phases are injected in the FFD using a syringe pump system (*Chemyx NanoJet*), equipped with three independent barrels and connected to the device with flexible Fluorinated Ethylene Propylene (FEP) tubing. The FFD (*Dolomite Microfluidics*) is fabricated along standard photolithography lines. The orifice of the flow-focusing junction is 14 μm deep and 17 μm wide. To store and manipulate the droplets, we designed and fabricated a separate device (ObC) with standard soft-lithography techniques. The ObC is made of two microscope coverslips separated by a PDMS film, approximately 30 μm in thickness. The FFD and ObC are connected through a flow splitter, which controls the flow fraction directed towards the ObC. Since the emulsion properties are temperature dependent, both FFD and ObC are fitted with on-chip temperature control systems, which consist of a resistance thermometer PT100, a Peltier cell and a temperature proportional-integral-derivative (PID) control unit (*Electron Dynamics Ltd. TC M PCB*). In all experiments the temperature is set to 25°±0.3°. Images of the devices were captured with an Olympus IX81 inverted microscope fitted with a *Q-Imaging Retiga EXi*. Image post processing for droplet sizing was performed with custom Java macros implemented in ImageJ.

Oil and aqueous solutions were pre-equilibrated before use. Heptane and dioctyl sulfosuccinate sodium salt (AOT) were mixed together through ultrasonic bath to obtain an oil solution with surfactant molar concentration c_{AOT}. Similarly, we prepared an aqueous solution of *Milli-Q* ultrapure water and sodium chloride at a molar concentration c_{NaCl}. The two solutions are combined and inverted three times. After ten minutes, the vial is inverted once more and left to settle overnight. All chemicals were used as received from *Sigma Aldrich*.

3.2 Trapping and manipulation

An inverted microscope is custom-built (*ThorLabs* components) with a piezo *xy*-stage (*Prior*) and *z*-actuator (*Zaber*) as a flexible alternative to commercial options. A 532 nm, 5W, TEM_{00} CW laser (*Laser Quantum*) is used, interchangeable with a 1070 nm 10W TEM_{00} CW single-mode fibre laser (*IPG*) alongside the appropriate antireflection optics and dichroic beamsplitter. These are collimated through beam expanders to overfill the ferroelectric SLM (*Forth Dimension*) or nematic SLM (*Hamamatsu*). Polarising beamsplitters and waveplates on the input and output are necessary for correct phase only operation of the FLC SLM. The diffractive output is demagnified to overfill the rear aperture of the microscope objective via an edge dichroic beamsplitter (*Razor-Edge, Semrock*). A high-performance water-immersion objective (Zeiss, C-Apochromat x63 NA 1.2) is chosen for its high numerical aperture, good transmission and aberration corrections over a wide wavelength range. We use Python libraries including a wxPython GUI. The holograms for 'lenses and prisms' point traps are calculated using Zernike terms for tilt and defocus before displaying on the SLM. Where Gaussian traps are effective on spherical droplets or fluorescent polystyrene beads (450 nm emission, 1-5 μm, *Polysciences*), brightfield images are processed in Python to facilitate trap strength calibration according to the power spectral method.[17]

3.3 Brightfield and epi-SIM imaging

The output of a 405nm, 1W LED (*ThorLabs*) is collimated and immediately passes through the structured illumination mask, joins the imaging train via a dichroic and is relayed into the object plane via matched achromats (f = 35mm) and the objective. The masking is implemented with a high-opacity Ronchi transmission grating (chrome on glass, *Applied Image*) at 50 μm/lp. This corresponds to a spatial frequency in the focal plane of $F = 1.3\ \mu m^{-1}$, chosen such that artefacts (for $N = 3$, introduced at $>4F$)[18] fall above the modulation transfer function (MTF) cutoff of 5.1 μm^{-1} and lose all contrast. In practice, the MTF of the system is confirmed as diffraction-limited by Fourier transforming the spatial derivative of a brightfield-imaged grating edge. This particular choice of grating allows the contrast, $m \sim 0.6$, to remain relatively high, whilst yielding a theoretical sectioning response near the optimal FWHM of ~0.4 μm. Using a second piezoactuator (*Zaber*) we move one of the achromats relative to the other to obtain images at axial step sizes of >0.2 μm and automate a SIM acquisition sequence over a 10 μm range. The CCD camera (*AVT Pike*) is used with a typical frame rate of 120 Hz, leading to sequence duration >2 s. Coding in Python allows RS232, IEEE1394, FireWire, USB and video control of each function to be de-centralised across an arbitrary computer network.

3.4 Photopolymerisation and confocal Raman spectroscopy

A 10 mW, 375nm, TEM_{00} CW laser (*Coherent*) is collimated into a pencil beam in order to bathe the focal volume in a quasi-uniform distribution (waist ~ 40 μm) of photoinitiating light on demand. Initiation light is continuous throughout polymerisation period of ~1s. Emulsions are prepared with water, AOT and NaCl (as §3.1**)**. Replacing heptane is the monomer isobornyl acrylate (IBA) and the photoinitiator of choice, 2,2-dimethoxy-2-phenylacetophenone (DMPA); both are acquired from *Sigma Aldrich*. A 100-μm pinhole (*ThorLabs*) corresponding to ±5 μm confocality is placed at the entrance of the spectrograph (*Shamrock, Andor*) coupled to a high aspect ratio, deep-cooled EMCCD (*Newton, Andor*) with frame rate ~1.5 kHz in crop mode.

4. MICROFLUIDIC PERFORMANCE

We now briefly describe the main features and performances of our microfluidic platform. A full characterization of the system will be reported elsewhere. The droplet formation is monitored for two values of the continuous phase flow rate Q_c, namely 1 µL/min and 10 µL/min. The ratio r between the flow rates of the continuous Q_c and dispersed phase Q_d is varied between 2 and 200. We generate droplets at the surfactant concentration, c_{AOT} =1mM, and salinity, c_{NaCl}=50mM, which correspond to the minimum of the interfacial tension for the examined oil-water-surfactant system at the experiment temperature.[19]

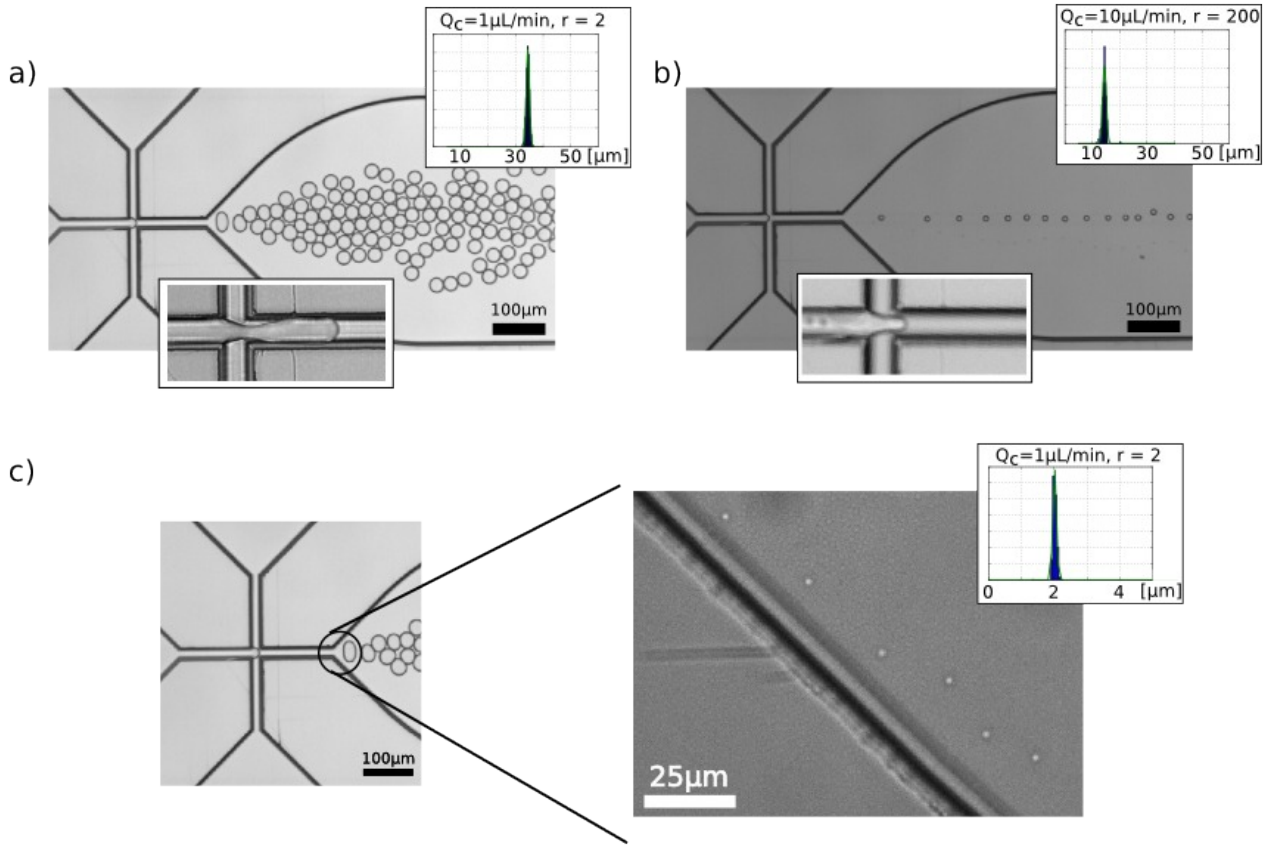

Figure 5. Droplet formation regimes and diameter histograms. Snapshots of droplet formation in (a) squeezing-like and (b) dripping-like regimes with close-ups of the junction (lower insets). Histograms of droplet diameters together with best-fit Gaussian curves are shown as well (upper insets). Mean diameters are 34.4±0.6 µm (c.v. 2%) and 14.5±0.7 µm (c.v. 5%), respectively. (c) 60x close-ups of the snapshot in panel (a) at the orifice exit, with the diameter histograms for the daughter droplets (inset). The average diameter given by the best-fit Gaussian curve is 2.0±0.06µm (c.v. 2.7%).

Two main droplet formation regimes are observed in all experiments. In the first regime, oil plugs are periodically formed at the junction and the resulting droplets are larger than the orifice (*Fig. 5a*). A very similar formation regime has been reported in literature for planar flow focusing geometries and it is referred to as a 'squeezing' regime.[20] The resulting droplets have a diameter ranging from 20-50 µm. In the second regime, the oil tongue at the junction tapers off at the entrance of the orifice and droplets, either similar or smaller than the orifice size, break off from the tongue tip (see *Fig. 5b*). That formation recalls the 'dripping' regime reported in literature for similar channel geometries.[20] Monodisperse droplets as small as 10µm in diameter can be generated in that regime. Those results show that the length scale of the device (namely, the orifice size) sets the length scale of the droplets, which is a few tens of micrometers.

However, to optically trap and deform ultra-low interfacial tension droplets, the optimal droplet diameter is in the range of 1-5μm. Unfortunately, the realization of devices with such a small orifice would require expensive and challenging fabrication processes. Even the operation of the device would be more complicated, since on-chip filters and anti-clogging systems have to be implemented.[21, 22]

Despite the fact that primary droplets are too large for the purposes of optical trapping, we observe that for both regimes, daughter droplets are generated simultaneously. Such droplets are an order of magnitude smaller than their counterparts and can be visualized only under high magnification. A close-up of the flow at the orifice exit is reported (*Fig. 5c*). Monodisperse droplet population with diameters between 2 - 4 μm are generated in such a regime. The droplet generation rate varies within the range from 0.5 - 15 kHz, according to the values of Q_c and r. Droplets are observed to preserve their size for several weeks once stored in airtight vials. Our microfluidic platform can manufacture monodisperse populations of ultra-low interfacial tension droplets, with the optimal size for optical trapping and manipulation, satisfactorily.

5. OPTICAL INTEGRATION

The complete optical design (*Fig. 6*) is intended such that five wavelength bands, corresponding to different functions, each follow a unique branch. These join a common path through the rear aperture of the objective, whose chromatic performance (UV-Vis-NIR) is crucial to retaining the simultaneous capabilities described above.

The ObC replaces the standard microscope sample between condenser and objective, and encompasses the field of view in which our experiments take place. The flow rates through the FFJ correspond to a fluid velocity of up to 100 μm s^{-1} in the ObC, so the flow splitter acts to isolate the ObC partially such that droplets can be captured and deformed under the dominance of optical forces. This also offers a passive method of droplet sorting. The microfluidic approach provides potentially very thin, flat sample chambers that are accessible with the high NA optics necessary for all the functions described. Devices are manufactured with glass or PDMS for general and predictable chemical and optical compatibility.

Table 3. Breakdown of optical inputs to and outputs from the ObC in the instrumental setup.

Waveband (nm)	Function	Major components
375	Photoinitiation of droplet polymerisation	UV laser
405	Fluorescent excitation with SIM masking	UV LED; grating; achromat relay
440-490	Fluorescent emission	Perylene fluorophore
470	Brightfield illumination	Blue LED
532 (or 1070)	Trapping beam	Green (NIR) laser; SLM
>532	Backscattered Raman signal	Spectrograph; pinhole; camera

Observing behaviour of particles in the ObC at micron scales or below requires an imaging technique with resolution comparable to the diffraction limit. The two such modes used here, brightfield and structured epi-illumination, are geometrically incompatible, though at different times they are easily combined and run under the same imaging optics. Together with the significant difference in acquisition speed, this implies that brightfield imaging is better for initial observations of trapping and other dynamic behaviour in 2D, whilst SIM is best used for highly stable objects on the occasion that 3D reconstruction is desired.

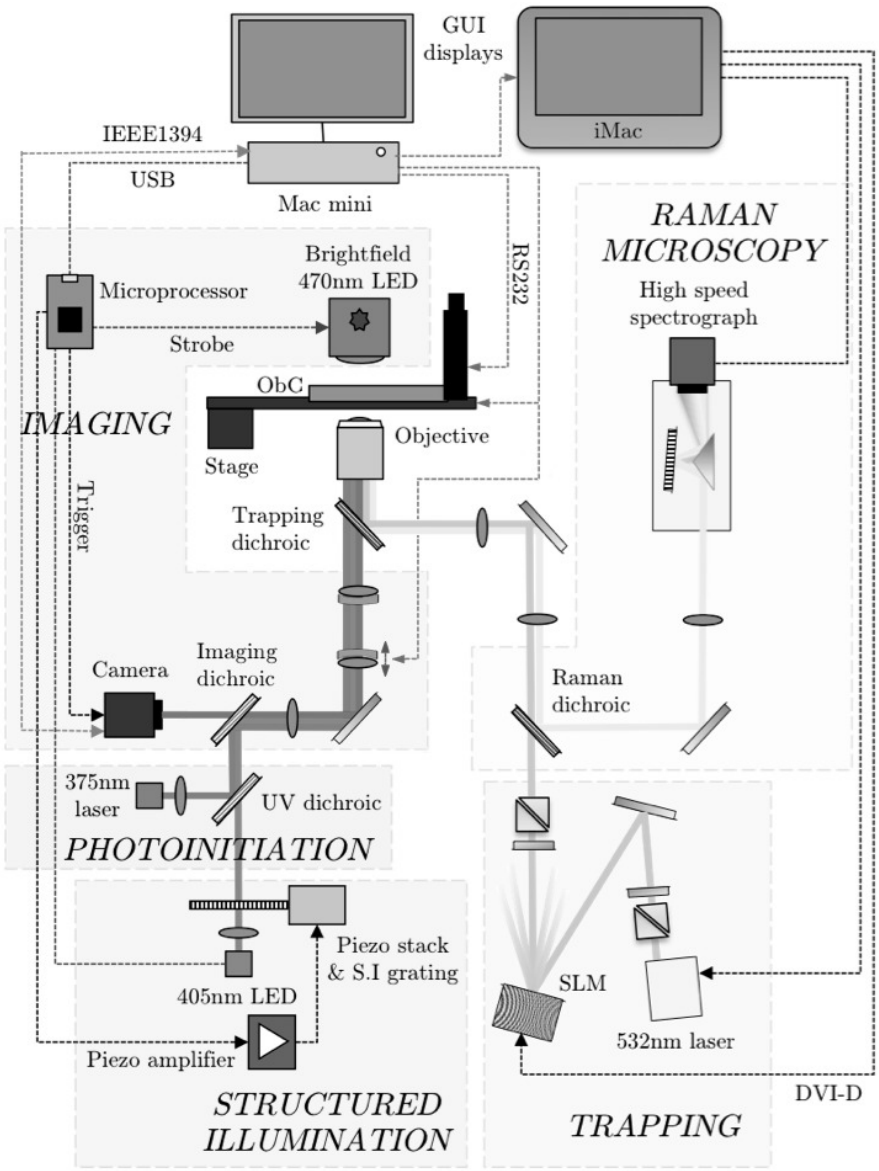

Figure 6. Schematic of the automated optical system comprising modules for production manipulation, interrogation and solidification of deformable microdroplets. ObC acts as microscope sample; FFJ and other microfluidic devices, not shown.

Trapping must allow objects to be held strongly enough so that they are effectively static over the course of a structured imaging routine. If detectable motion were periodic for some reason, such as vibrational or rotational motion, then strobing the illumination would be an acceptable solution. However, weakly held or untrapped objects will instead blur images under stochastic diffusive motion. This leads to the appearance of random transverse discontinuities and significant uncertainty in the sampled interval (*Fig. 7*). By equipartition, the minimum trap strength to preserve diffraction limited imaging at 4σ performance (i.e. discontinuity-free over 100 routines of 50 sections each) is:

$$\kappa > 4^2 \frac{k_B T}{\left(\lambda / 2NA\right)^2} \sim 10^{-6}\,\mathrm{Nm}^{-1}, \tag{3}$$

which is easily achieved. This can be an underestimate in practical microfluidics where external influences such as

hydrodynamic fluctuations increase the probability of the maximum displacement becoming detectably large. Notably, a shorter SIM duration t truncates sampling of the displacement distribution. If we represent such a drift in continuous fluid velocity averaged over this time as $\dot{v}$, a more realistic requirement is:

$$\kappa > \frac{\beta \dot{v} t}{\lambda / 2NA}. \tag{4}$$

This is largely limited by the camera frame rate and the ability to avoid pressure gradients, particularly from syringe motion and elasticity in piping and PDMS.

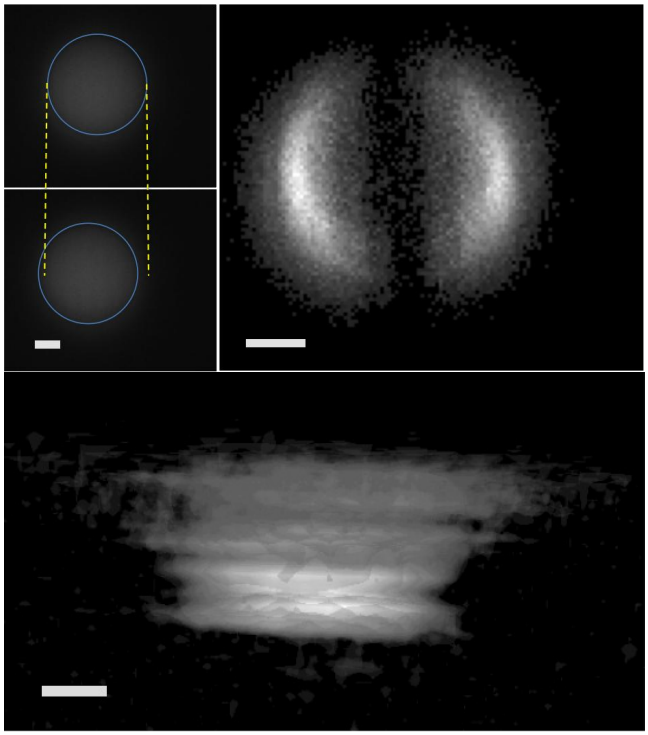

Figure 7. Examples of fluorescent SIM artefacts generated by Brownian motion of a large, untrapped dodecane droplet (20 µm diameter) in water at high surface tension, compressed into an approximately cylindrical shape between coverslip and microscope slide; (top left) a pair of consecutive sectioned images at different z showing noticeable x displacement; (top right) the differential variance between the two z-sections, highlighting the region of uncertainty in x; (bottom) the xz profile of the reconstructed cylindrical volume, showing more transverse discontinuities and additional noise near the flattened faces due to uncertainty in z. Scale bars = 5 µm.

Use of the trapping laser as a Raman probe is a powerful strategy where particle composition is of interest. The high numerical aperture optics required for the former enhance the signal from the latter, whilst Raman detection has little impact on the optics or methodology of tweezing.[23] Using 'Raman tweezers' removes the need for a separate laser and its unwanted additional radiation pressure. Also, a single longitudinal mode laser is unnecessary, since a suitable laser bandwidth is an order less than the typical spectral linewidth, typically ~100 GHz. In this scheme, the Raman signal and gradient forces are coupled through the input intensity distribution, such that a minimum trapping power is required for sufficient spectral output. Much like the stability issue with SIM, as long as this minimum power falls below that required to trap the object of interest, then Raman spectroscopy can be performed without hindrance. By the same token, structuring the Raman probe is clearly not an option when trapping, so instead a more subtle confocality is established with the spectrometer's spatial filter. The photopolymerisation pump is not expected to conflict with trapping, imaging or Raman with the appropriate optical filters, since the changes in fluorescent return or refractive index on polymerisation are small. The construction of thread networks in this instrument is an exciting prospect: on an attolitre scale, the

chemistry of individual molecules is within reach. Facilitating Raman spectroscopy *in situ* is therefore a significant goal for probing reaction chemistry as well.

In this framework, it is possible to perform brightfield imaging and Raman spectroscopy simultaneously on trapped, deformed and polymerised microdroplets. On the other hand, fluorescence is often described as anathema to Raman microscopy due to the higher fluorescent cross-sections. In samples doped with fluorophore it is likely that it will overwhelm the Raman signal even at wavelengths distant from peak emission. Besides this, the effective frame rate in the structured illumination technique falls far short of resolving the droplet polymerisation on sub-second timescales. However, effective combination with widefield fluorescence imaging is thought possible if emission bands are sufficiently weak at the probe laser wavelength, and structured illumination also if processes sufficiently longer than the acquisition time are interrogated. It is possible to conceive of adjacent modules that would perform such conflicting functions in parallel on separate client particles, thus forming a multi-step production line of arbitrary complexity. A simple extension of the microfluidic framework, as employed between FFD and ObC, would facilitate transport between these steps.

6. CONCLUSIONS

A multi-faceted instrument for the complete production, optical deformation, polymerisation, and characterisation of both composition and morphology of ultralow surface tension microdroplets has been presented. Having considered the benefits and drawbacks of each technique alone and in parallel, we have successfully integrated them. The instrument's experimental performance has been effective in the production stage, with a satisfactory projection for the available optical techniques. The progress and combined performance of all five functions are ongoing concerns for future publication.

We hope that such an instrument will lead to the development and mass production of arbitrary microparticles, which could act as building blocks for optical waveguides or micromachinery. The demand for a greater range of sizes and shapes of non-spherical particles is likely to grow as more applications are found. In addition, it will facilitate the production of 3D optically stabilised emulsion networks, providing a nanofluidic laboratory to investigate physicochemical behaviour in fluids on a molecular scale.

7. ACKNOWLEDGEMENTS

Many thanks to Dr David Woods, Oliver Burnham, Dr. Lian Hutchings, David Tapp, Dr. Buddhapriya Chakrabarti, Dr. Jonathan Taylor and Dr Xize Niu for their contributions to related research in the OPTONANOFLUIDICS collaboration. Thanks and congratulations also to Dr. Christopher Saunter, architect of our Python framework. This work is funded by the Engineering and Physical Sciences Research Council (EPSRC), UK.

8. REFERENCES

[1] Seemann, R., Brinkmann, M., Pfohl, T. *et al.*, "Droplet based microfluidics," Reports on Progress in Physics, 75(1), (2012).
[2] Huebner, A., Sharma, S., Srisa-Art, M. *et al.*, "Microdroplets: A sea of applications?," Lab on a Chip, 8(8), 1244-1254 (2008).
[3] Lee, K. J., Yoon, J., and Lahann, J., "Recent advances with anisotropic particles," Current Opinion in Colloid & Interface Science, 16(3), 195-202 (2011).

[4] Solvas, X. C. I., and deMello, A., "Droplet microfluidics: recent developments and future applications," Chemical Communications, 47(7), 1936-1942 (2011).
[5] Woods, D. A., Mellor, C. D., Taylor, J. M. *et al.*, "Nanofluidic networks created and controlled by light," Soft Matter, 7(6), 2517-2520 (2011).
[6] Ward, A. D., Berry, M. G., Mellor, C. D. *et al.*, "Optical sculpture: controlled deformation of emulsion droplets with ultralow interfacial tensions using optical tweezers," Chemical Communications(43), 4515-4517 (2006).
[7] McGloin, D., "Optical tweezers: 20 years on," Philosophical Transactions of the Royal Society a-Mathematical Physical and Engineering Sciences, 364(1849), 3521-3537 (2006).
[8] Thalhammer, G., Bowman, R. W., Love, G. D. *et al.*, "Speeding up liquid crystal SLMs using overdrive with phase change reduction," Opt. Express, 21(2), 1779-1797 (2013).
[9] Spalding, G. C., Courtial, J., and Di Leonardo, R., Chapter 6 - Holographic Optical Tweezers, [Structured Light and Its Applications], ed. David, L. A., Academic Press, Burlington, 139-168 (2008).
[10] Neil, M. A. A., Juskaitis, R., and Wilson, T., "Method of obtaining optical sectioning by using structured light in a conventional microscope," Optics Letters, 22(24), 1905-1907 (1997).
[11] Hagen, N., Gao, L., and Tkaczyk, T. S., "Quantitative sectioning and noise analysis for structured illumination microscopy (vol 20, pg 403, 2012)," Optics Express, 20(5), 5343-5343 (2012).
[12] Heidingsfelder, P., Gao, J., and Ott, P., "Theoretical analysis of photon noise limiting axial depth resolution for three-dimensional microscopy by incoherent structured illumination," Optical Engineering, 51(10), (2012).
[13] Hagen, N., Gao, L., and Tkaczyk, T. S., "Quantitative sectioning and noise analysis for structured illumination microscopy," Opt. Express, 20(1), 403-413 (2012).
[14] Ward, A. D., Berry, M., Ash, P. *et al.*, "The polymerisation of emulsion droplets deformed using laser tweezers to create microscopic polymer particles," Central Laser Facility Annual Report, 199-201 (2006).
[15] Van de Sompel, D., Garai, E., Zavaleta, C. *et al.*, "A Hybrid Least Squares and Principal Component Analysis Algorithm for Raman Spectroscopy," Plos One, 7(6), (2012).
[16] Dieing, T., and Hollricher, O., "High-resolution, high-speed confocal Raman imaging," Vibrational Spectroscopy, 48(1), 22-27 (2008).
[17] Berg-Sorensen, K., and Flyvbjerg, H., "Power spectrum analysis for optical tweezers," Review of Scientific Instruments, 75(3), 594-612 (2004).
[18] Schaefer, L. H., Schuster, D., and Schaffer, J., "Structured illumination microscopy: artefact analysis and reduction utilizing a parameter optimization approach," Journal of Microscopy-Oxford, 216, 165-174 (2004).
[19] Aveyard, R., Binks, B. P., Clark, S. *et al.*, "Interfacial-Tension Minima in Oil-Water Surfactant Systems - Behavior of Alkane Aqueous Nacl Systems Containing Aerosol Ot," Journal of the Chemical Society-Faraday Transactions I, 82, 125-142 (1986).
[20] Lee, W., Walker, L. M., and Anna, S. L., "Role of geometry and fluid properties in droplet and thread formation processes in planar flow focusing," Physics of Fluids, 21(3), (2009).
[21] Candiani, G., Del Curto, B., Malloggi, C. *et al.*, "Development of novel cardboard filters very effective in removing airborne bacteria from confined environments," Journal of Applied Biomaterials & Biomechanics, 9(3), 207-213 (2011).
[22] Shui, L. L., van den Berg, A., and Eijkel, J. C. T., "Scalable attoliter monodisperse droplet formation using multiphase nano-microfluidics," Microfluidics and Nanofluidics, 11(1), 87-92 (2011).
[23] Ajito, K., and Torimitsu, K., "Near-infrared Raman spectroscopy of single particles," TrAC Trends in Analytical Chemistry, 20(5), 255-262 (2001).